Correspondence to:

M. Colombier,
mathieu.colombier@min.uni-muenchen.de

Pre-Eruptive Outgassing and Pressurization, and Post-Fragmentation Bubble Nucleation, Recorded by Vesicles in Breadcrust Bombs From Vulcanian Activity at Guagua Pichincha Volcano, Ecuador

M. Colombier[1] , M. Manga[2] , H. Wright[3], B. Bernard[4] , R. deGraffenried[5] , F. Cáceres[1] , P. Samaniego[4,6] , J. Vasseur[1] , K. Jakata[7], P. Cook[7], and D. B. Dingwell[1]

[1]Department of Earth and Environmental Sciences, Ludwig-Maximilians-Universität München, München, Germany, [2]University of California, Berkeley, Berkeley, CA, USA, [3]U.S. Geological Survey, Volcano Disaster Assistance Program, Vancouver, WA, USA, [4]Instituto Geofísico, Escuela Politécnica Nacional, Quito, Ecuador, [5]School of Earth and Space Exploration at Arizona State University, Tempe, AZ, USA, [6]Laboratoire Magmas Et Volcans, Université Clermont Auvergne, CNRS, IRD, OPGC, Clermont-Ferrand, France, [7]Engineer, ESRF-The European Synchrotron, Grenoble, France

Abstract Breadcrust bombs formed during Vulcanian eruptions are assumed to originate from the shallow plug or dome. Their rim to core texture reflects the competition between cooling and degassing timescales, which results in a dense crust with isolated vesicles contrasting with a highly vesicular vesicle network in the interior. Due to relatively fast quenching, the crust can shed light on pre- and syn-eruptive conditions prior to or during fragmentation, whereas the interior allows us to explore post-fragmentation vesiculation. Investigation of pre- to post-fragmentation processes in breadcrust bombs from the 1999 Vulcanian activity at Guagua Pichincha, Ecuador, via 2D and 3D textural analysis reveals a complex vesiculation history, with multiple, spatially localized nucleation and growth events. Large vesicles (Type 1), present in low number density in the crust, are interpreted as pre-eruptive bubbles formed by outgassing and collapse of a permeable bubble network during ascent or stalling in the plug. Haloes of small, syn-fragmentation vesicles (Type 2), distributed about large vesicles, are formed by pressurization and enrichment of volatiles in these haloes. The nature of the pressurization process in the plug is discussed in light of seismicity and ground deformation signals, and previous textural and chemical studies. A third population (Type 3) of post-fragmentation small vesicles appears in the interior of the bomb, and growth and coalescence of Type 2 and 3 vesicles causes the transition from isolated to interconnected bubble network in the interior. We model the evolution of viscosity, bubble growth rate, diffusion timescales, bubble radius and porosity during fragmentation and cooling. These models reveal that thermal quenching dominates in the crust whereas the interior undergoes a viscosity quench caused by degassing, and that the transition from crust to interior corresponds to the onset of percolation and development of permeability in the bubble network.

Plain Language Summary Breadcrust bombs are volcanic ejecta formed during explosive volcanic eruptions by rapid cooling of the exterior (the crust) and slow cooling of the interior that causes gas loss, bubble growth and cracking of the exterior. The rapidly cooled crust preserves characteristics of the magma prior to explosion. We study here the variations in porosity and vesicle properties from crust to interior in breadcrust bombs from the Guagua Pichincha volcano in Ecuador. Our results shed light on the pre-eruptive conditions in the magma prior to explosive activity, and on the post-fragmentation evolution of the bomb interior by bubble formation.

1. Introduction

Vulcanian eruptions are short-lived, discrete explosive volcanic events that can generate high eruptive plumes, ballistic fallout, as well as pyroclastic flows and surges (Clarke et al., 2015; Druitt et al., 2002). One model for conduit processes that lead to Vulcanian activity involves the formation of a dense plug or dome by outgassing, underneath which gas-rich magma is injected with limited volatile loss. Fragmentation and explosions can then be driven by a combination of (a) dome-collapse causing decompression of magma in the conduit and (b) over-pressure and brittle-fragmentation of the magmatic foam beneath this plug/dome (Druitt et al., 2002). A fragmentation front propagates downward through this vertically heterogenous conduit. Due to their low volatile content,

Visualization: M. Colombier, B. Bernard
Writing – original draft: M. Colombier
Writing – review & editing: M. Colombier, M. Manga, H. Wright, B. Bernard, R. deGraffenried, F. Cáceres, P. Samaniego, J. Vasseur, K. Jakata, P. Cook, D. B. Dingwell

blocks originating from the uppermost conduit and dome are minimally modified during explosions, whereas volatile-rich breadcrust bombs from lower parts of the plug and pumice clasts from the magma underneath the plug experience syn- and post-fragmentation textural modifications via bubble nucleation, growth, and coalescence (Giachetti et al., 2010, 2011; Wright et al., 2007).

Breadcrust bombs originating from the top of the conduit enter the air immediately after fragmentation and hence experience higher cooling rates than pyroclasts from the deeper conduit (Giachetti et al., 2010). Such bombs thus preserve a rapidly quenched dense crust with little to no post-fragmentation textural change. In contrast, the core of breadcrust bombs dwells at a temperature significantly higher than the glass transition temperature for long enough to evolve texturally as bubbles nucleate and grow, yielding the possibility of the formation of an interconnected and permeable network of bubbles. In this manner, vesicularity gradients in breadcrust bombs are controlled by the relative timescales of cooling and vesiculation, which are in turn influenced by initial water contents and pyroclast transport mechanisms (e.g., projectile or pyroclastic density currents; Benage et al., 2014). Breadcrust bombs can therefore provide key information about (a) pre-eruptive textural, chemical (volatile content), and pressure conditions in the conduit at the time of, and before, fragmentation, (b) links between cooling history of the bomb and dynamics of bubble formation, and (c) the transition from closed- to open-system degassing in magma at near-atmospheric pressure and in the presence of variable amounts of crystals.

Here, we investigate breadcrust bombs formed during the 1999 Vulcanian explosions of Guagua Pichincha volcano, Ecuador. Wright et al. (2007) have already qualitatively described a vesiculation pattern in these breadcrust bombs which is heterogenous with respect to axes parallel and perpendicular to the crust. Here, we quantify the evolution of porosity, vesicle number density (VND), and vesicle size distribution (VSD) parallel and perpendicular to radial profiles for breadcrust bombs from Guagua Pichincha. Using textural analysis of different vesicle populations along these profiles, we aim to: (a) derive key information on bubble nucleation, growth and coalescence processes from magma ascent in the conduit to bomb ejection and transport, (b) make the link between vesicle textures and pressurization processes during Vulcanian eruptions, and (c) more broadly, increase our current knowledge of degassing and permeability development in crystal-rich silicic magmas. We find that large vesicles preserved in the crust are due to an early outgassing and bubble collapse event prior to fragmentation, whereas small vesicles record syn- and post-fragmentation vesiculation and development of permeability in the bombs. Haloes of small vesicles around a larger population observed in the crust have implications for pre-eruptive conduit pressurization and fragmentation in the dome/plug region and can be interpreted in the light of seismic and ground deformation signals. We also study the link between cooling and post-fragmentation vesiculation by examining viscosity evolution, bubble growth rates, and diffusion timescales.

2. Materials and Methods

2.1. 2D Textural Analysis

We studied two breadcrust bombs (GP8 and GP10 described in Wright et al., 2007) formed during 1999 Vulcanian eruptions at Guagua Pichincha volcano, Ecuador. The reader is referred to Wright et al. (2007, 2023) for a detailed description of the Vulcanian activity and associated deposits. Hereafter, we refer to groundmass as regions of the samples outside of micro-phenocrysts and phenocrysts and that include glass, small vesicles, and microlites. The limit between microlites and micro-phenocrysts/phenocrysts was set at 30 μm (Colombier et al., 2022).

Samples were prepared in two ways for 2D textural analysis. First, we drilled a 14 mm high and 5 mm wide cylinder from rim to core in sample GP8. This cylinder was then cut every 1 mm along planes parallel to a given radial position (R) from $R = 0$ (crust) to $R = 14$ mm (interior) using a 200-μm-thick, diamond-coated wire saw, resulting in 15 slices. This first approach allowed us to evaluate lateral heterogeneities at a given value of R. Slices of known radial distance were impregnated into an epoxy mount and then polished. This strategy contributed some error in the measurement of R that we estimate to ± 0.1 mm. The second approach was to prepare a thin section parallel to a rim-core profile (perpendicular to the crust surface) in sample GP8 to exclude any error on radial position and to obtain textural parameters directly at the outermost part of the crust.

Back-scattered electron (BSE) images at different magnifications were taken on a HITACHI SU 5000 Schottky FE-SEM (Scanning Electron Microscope) at the Ludwig Maximilians University (LMU, Germany). We used images at high magnification (X2500, on areas of $\sim 2 \times 10^{-3}$ mm^2) to quantify local values of vesicle number

density for small vesicle populations and to account for heterogeneities. We focus with this method on small vesicles in order to see the localized evolution of degassing in the groundmass, whereas a statistical analysis of large vesicles required 3D analysis using Synchrotron-sourced X-ray microtomography due to their lower abundance and distributions over large volumes. The cut-off diameter of small vesicles depends on the location in the samples and is <10 μm in the crust and <50 μm in the interior. Four images were taken at different locations for each given radial position at this magnification. These images were binarized, vesicles were manually decoalesced and VSD and VND were obtained from 2D to 3D stereological conversion using FOAMS software (Shea et al., 2010). All values for VND and VSD given hereafter are corrected for micro-phenocrysts, phenocrysts, and porosity.

In order to validate this method focused on localized values of vesicle properties at high magnification, we compare the VSD and VND for analysis on such small areas and the ones obtained using four different magnifications (larger total areas of $\sim$3.5 mm^2) and including all images at the highest magnification. The VND obtained with four magnifications is 1×10^7 mm^{-3}, which falls in the range obtained using single images at the highest magnification (8×10^6–7×10^7 mm^{-3}), and the overall distribution is similar.

2.2. 3D Analysis Using Synchrotron-Sourced X-Ray Microtomography

3D analysis was performed on two cylinders of 5 mm diameter and $\sim$20 mm length drilled in two breadcrust bombs (GP8 and GP10; Wright et al., 2007). The two samples were first scanned with a voxel size of 2.5 microns in order to image the entire cylinder across the rim-core transition and to image the population of large vesicles. The VND of large vesicles was measured up to a distance of 2.75 mm from the crust (volume of $\sim$21 mm^3) in order to yield values closest to the pre-eruptive conditions but still in a representative volume. Further, one breadcrust bomb was imaged in more detail in different areas along the radial profile at a voxel size of 360 nm. We note that this voxel size is still not small enough to quantify the 3D VND and was only used to obtain qualitative textural features such as imaging the halo of small vesicles around large ones.

Tomographic scans were performed at ESRF BM05 using a filtered white beam. Scans with a 2.5 μm voxel size were performed with 2.3 mm Al, 0.1 mm Mo, and 50 mm SiO$_2$ filters, resulting in an average energy of 80 keV. The detector used was developed in-house using a zoom lens coupled to a PCO Edge 4.2 CLHS (PCO Excelitas GmbH, Kelheim, Germany) and a lutetium aluminum garnet (LuAG) scintillator. Data collection was performed with 30 ms exposure at a nominal ring current of 200 mA in either full acquisition mode over 2,999 projections or half-acquisition with 4,000 or 4,500 projections per tomographic scan. Scans at 360 nm voxel size were performed with 2.3 mm Al and 0.24 mm Mo filters, resulting in an average incident energy of 74 keV. The TwinMic detector (Optique Peter, Lentilly, France) used a PCO Edge 4.2 CLHS (PCO Excelitas GmbH, Kelheim, Germany) with a specially shielded Mitutoyo Plan Apo 10X long-working-distance, infinity-corrected, objective lens (Optique Peter, Lentilly, France) coupled to an 8.8-μm-thick lutetium oxyorthosilicate (LSO) scintillator. Data collection was performed with exposure times of 150 or 320 ms at a nominal ring current of 32 mA in half-acquisition mode with 6,000 projections per tomographic scan. 3D volumes were visualized and quantified using Avizo (https://www.thermofisher.com/de/de/home/industrial/electron-microscopy/electron-microscopyin-struments-workflow-solutions/3d-visualization-analysissoftware.html).

3. Results

The breadcrust bombs show heterogeneities in vesicle number and size (a) along rim-core profiles with increases in both properties (and subsequently in porosity) toward the core (Figure 1) and (b) in planes perpendicular to radial orientation, that is at fixed values of R as previously mentioned by Wright et al. (2007) (Figure 2). Abundant cracks and voids in crystals (Figure 1) also contribute to porosity and pore connectivity in these samples but these types of pores are omitted in this study since we focus on vesiculation processes.

We can distinguish three main distinct vesicle populations: (a) Type 1 are large vesicles, tens to hundreds of microns in diameter, observed both in rims and cores (Figures 1, 3 and 4); (b) Type 2 are small vesicles (hundreds of nanometers to tens of microns) forming haloes surrounding large Type 1 vesicles in the crust (Figure 4); and (c) Type 3 are small vesicles (few to tens of microns in diameter) that nucleated and grew in groundmass areas outside of Type 1–2 clusters. The boundary between haloes of Type 2 vesicles and Type 3 vesicles cannot be distinguished in the core due to the high porosity and similar vesicle sizes (Figure 2). We also identified a fourth type
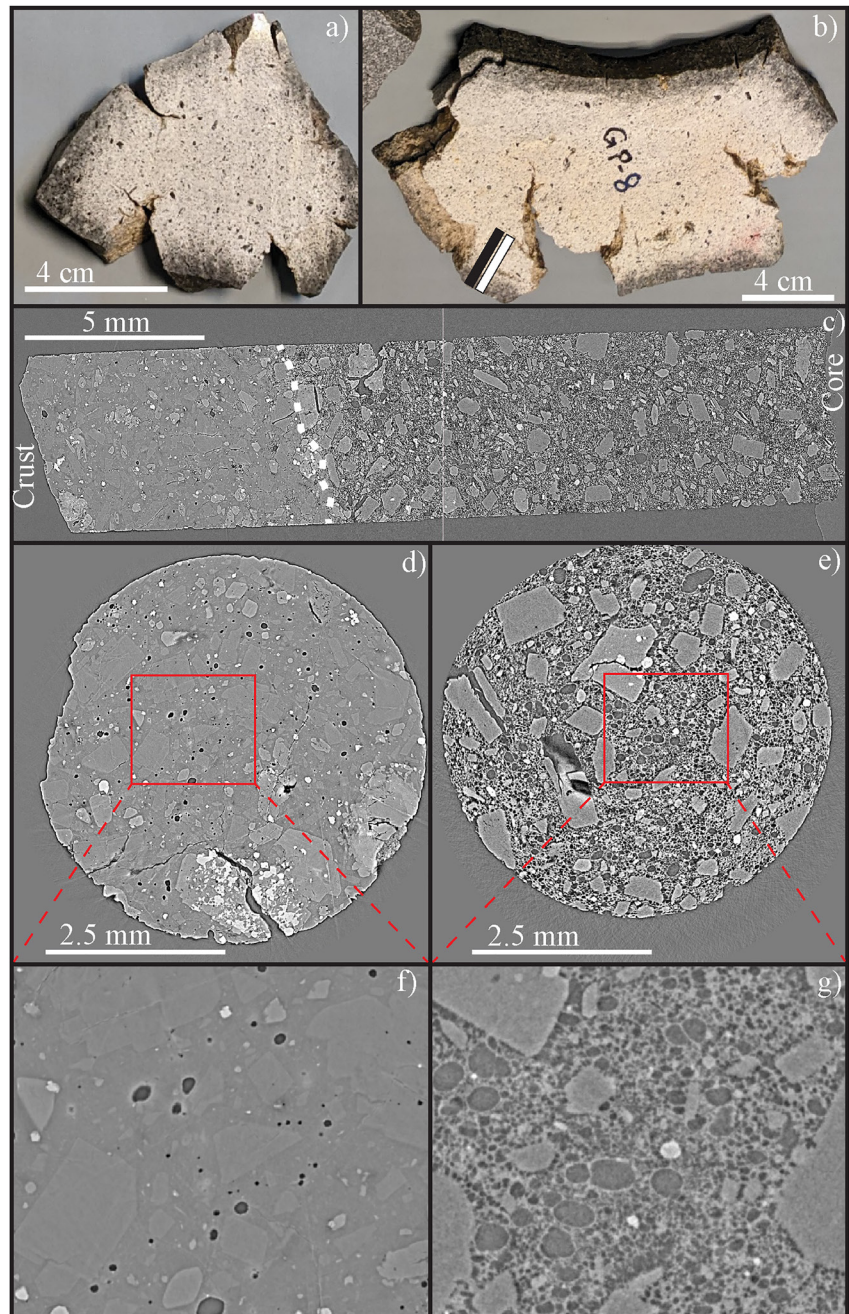
Figure 1. Rim to core texture of the two breadcrust bombs studied here. (a and b) Photographs of bombs GP8 and GP10 showing the macroscopic rim (gray and dense) to core (white and porous) transition. The black and white rectangles in (b) mark the location of the cylinders in GP8. (c to g) Synchrotron-sourced X-ray microtomography images of a cylinder cored in bomb GP8. Vesicles are black, glass is gray and crystals are gray to white. (c) Textural evolution from rim to core. The dashed line is to guide the eye toward the crust-interior transition at a radial position of ~6–7 mm. (d) Typical texture observed in the crust of GP10 with large, isolated Type 1 vesicles with a size of tens of microns up to hundreds of microns (see zoom in f). (e) Typical texture in the core of GP10, with a bimodal vesicle distribution consisting of large Type 1 vesicles surrounded by a groundmass with small, Type 2 and 3 vesicles (zoom in g). Note the increase in size of the large vesicles from crust (f) to the core (g).

of vesicle that is few microns to tens of microns and organized as vesicle trains surrounding micro-phenocrysts (Figure 5). These vesicles may correspond to Type 1–2 haloes but the enhanced coalescence around crystals makes them more difficult to identify and measure. Therefore, those type 4 vesicles will not be discussed further.
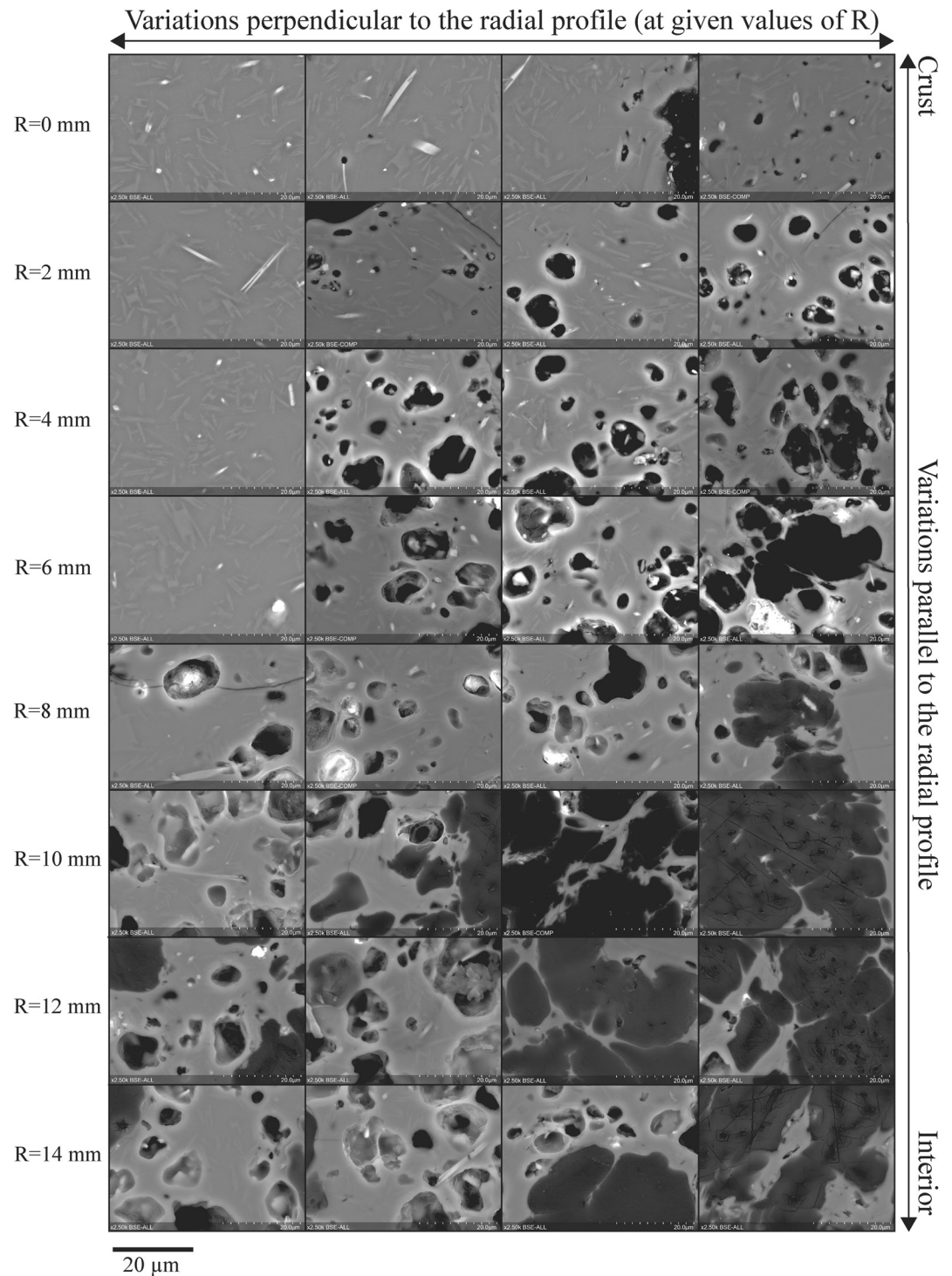
Figure 2. Back-scattered electron (BSE) images showing the micro-scale textural variations, related to small Type 2 and 3 vesicle populations, both parallel and perpendicular to the radial profile in the bomb GP8. R is the radial distance beneath the surface of the crust in millimeters. Images were taken to capture heterogeneities in the groundmass at a given R, are all at the same magnification and scale, and are organized by increasing apparent porosity and number density from left to right at a given value of R. We do not discriminate between Type 2 and 3 vesicles here, but we note that vesicles in the crust from $R = 0$–6 mm consist mostly of Type 2 vesicles.
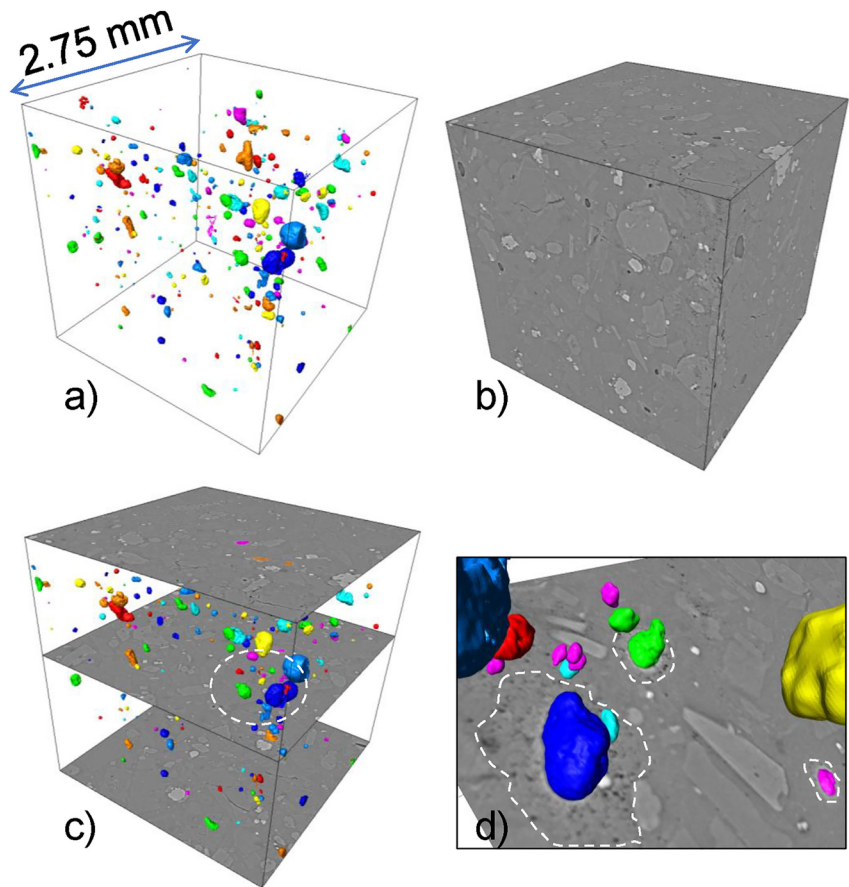
Figure 3. Synchrotron-sourced X-ray microtomography with a voxel dimension of 2.5 µm showing the distribution of the large, Type 1 vesicles in the crust. (a) 3D volume rendering showing individual, large Type 1 vesicles in the crust. (b) 3D volume rendering showing the gray scale contours of the cropped area, illustrating the dense nature of the crust (vesicles appear in black, crystals and glass in different gray tones). (c) 3D volume rendering of the spatial distribution of Type 1 vesicles, combined with grayscale 2D slices, with the dashed circle identifying the magnified area shown in (d) in a different orientation. (d) Zoom of the Type 1–2 halos of vesicles of (c) with the limit between large 3D vesicles and 2D, intersecting Type 2 vesicles in the halos identified with white dashed curves.

Type 1 vesicles seem to show an overall increase in size from rim to core (Figures 1f and 1g) but are distributed rather homogeneously along radial profiles. The VND of Type 1 in the first three millimeters of the crust has a value of $\sim 10^1$ mm^{-3} (Figures 3 and 6). These large vesicles are systematically surrounded by a halo of Type 2 vesicles (Figures 3 and 4), with a VND several orders of magnitude higher at $\sim 10^7$ mm^{-3} (Figure 6). In the crust, areas outside of these Type 1–2 clusters are vesicle-free. The relative area of vesicle-free groundmass decreases toward the core of the bombs, and vesicle-free groundmass in the entire analyzed area ($\sim 2 \times 10^{-3}$ mm^2) is no longer found at $R > 6$ mm (Figure 2). This is due to the nucleation and growth of Type 3 vesicles. The vesicle number density of small vesicles (Type 2 and/or Type 3) toward the core has a range of $\sim 10^{6-7}$ mm^{-3} (Figure 6). Due to the progressive increase in size and abundance of Type 2 and 3 vesicles toward the core, coupled to the increase in size of Type 1 vesicles and loss of vesicle-free groundmass areas, there is an overall increase in porosity and VND from rim to core. However, we stress that local values of porosity and VND are more relevant here and vary greatly at a given radial distance (Figures 6a, 6b, and 6d). The local groundmass VND at the crust ranges from zero (in vesicle-free areas) to up to 10^7 mm^{-3} in halos (Figure 6).

We can separate groundmass vesicles into three groups: (a) isolated, (b) coalesced, and (c) connected, where vesicle coalescence spans the whole image size. The term connected relates here more to a high degree of local coalescence rather than a system-spanning permeable network. There is an overall correlation between VND and porosity and both parameters increase from isolated to coalesced with maximum values reached in connected networks (Figure 6c).
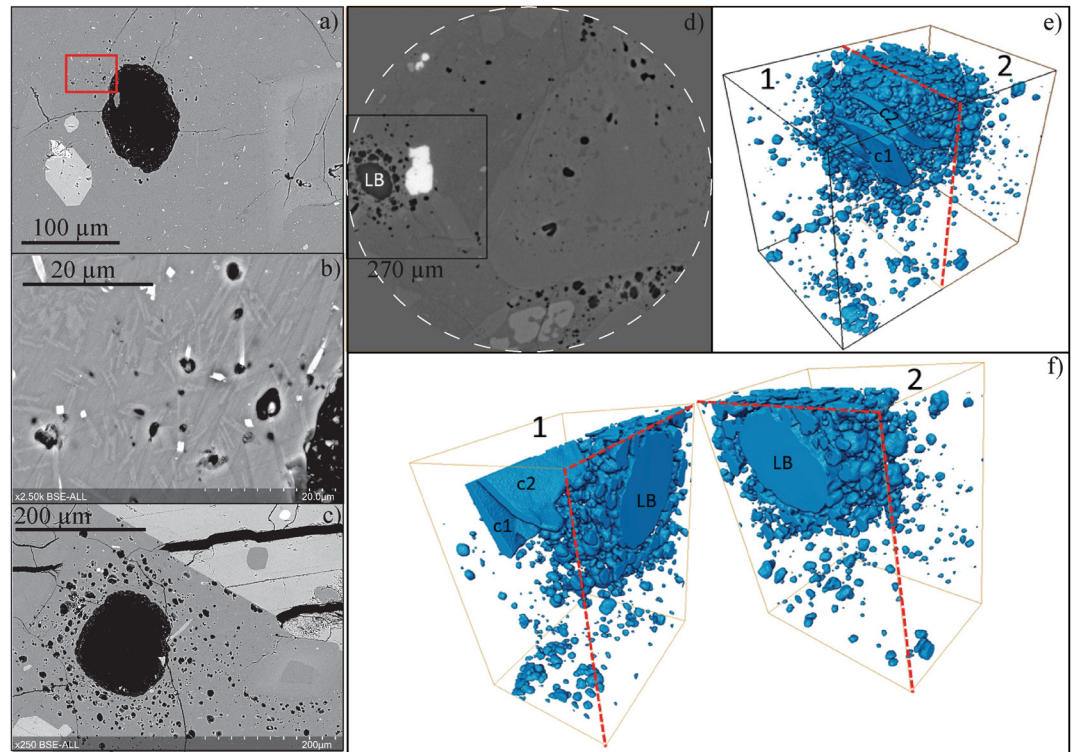
Figure 4. Haloes of small Type 2 vesicles around large, Type 1 vesicles. (a) Back-scattered electron image of a halo with a zoom-in region (red box) shown in (b). (c) Back-scattered electron image of a Type 1–2 cluster surrounded by micro-phenocrysts. (d) 2D slice of the synchrotron-sourced X-ray microtomography image at a voxel size of 360 nm showing a halo of Type 2 vesicles around a larger Type 1 vesicle. The white dashed line is to guide eye on the limits of the scanned area of the sample at this magnification. Note that the groundmass area outside of the Type 1–2 cluster is vesicle-free. (e) 3D volume rendering corresponding to the outlined area of (d) (black square) and showing the halo of small Type 2 vesicles and vesicle-poor groundmass surrounding this halo. (f) Internal view of the Type 1–2 cluster shown in (e) and separated in two parts across the red dashed line, revealing the presence of the large Type 1 vesicle (LB) surrounded by the halo of Type 2 vesicles. c1 and c2 in (e) and (f) correspond to cracks within crystals, one of these being also observed in 2D in (d) on the bottom left area of the large vesicle.

Porosity evolution with radial distance shows that connected areas are mostly found at a groundmass porosity >0.5 and up to ~0.8 (except one sample at lower values due to vesicle stretching in this area) (Figure 6d). These values straddle or are in excess of the range of percolation thresholds (the transition from an isolated/coalesced vesicle network to system spanning connectivity and onset of permeability, hereafter noted Φ_c) in the groundmass that have been discussed for these breadcrust bombs by Colombier et al. (2022) based on the model of Giachetti et al. (2019) (Figure 6d). In addition, groundmass porosity values in the bomb interiors fall just above this porosity threshold (Wright et al., 2007). We note that Φ_c is reached locally at different radial positions across the sample. We also find no connected areas near the crust where $R < 6$ mm, which also corresponds to the zone where vesicle-free groundmass is observed (Figure 6d).

We observe a bimodal vesicle size distribution both in the rim and the core (Figure 7). These VSDs illustrate the temporal evolution of vesicle populations with first the formation of Type 1 vesicles (large mode in Figures 7 and 7b) and addition of a small mode of surrounding Type 2 vesicles (Figures 7a and 7b). Toward the core, Type 3 vesicles are also present and contribute to the small mode with Type 2 vesicles, and both small and large modes are then shifted to larger diameters due to a combination of growth, coalescence, and expansion (Figure 7c). An exponential fit for both small and large vesicle distributions is observed in the crust, illustrating a process of continuous nucleation (Blower et al., 2003) (Figure 7a). An exponential fit is also observed for vesicles smaller than 10 µm in the interior. Larger vesicles in the interior have neither exponential nor power law distributions due to the influence of multiple processes on the VSD (nucleation, growth, and coalescence) (Figure 7a).
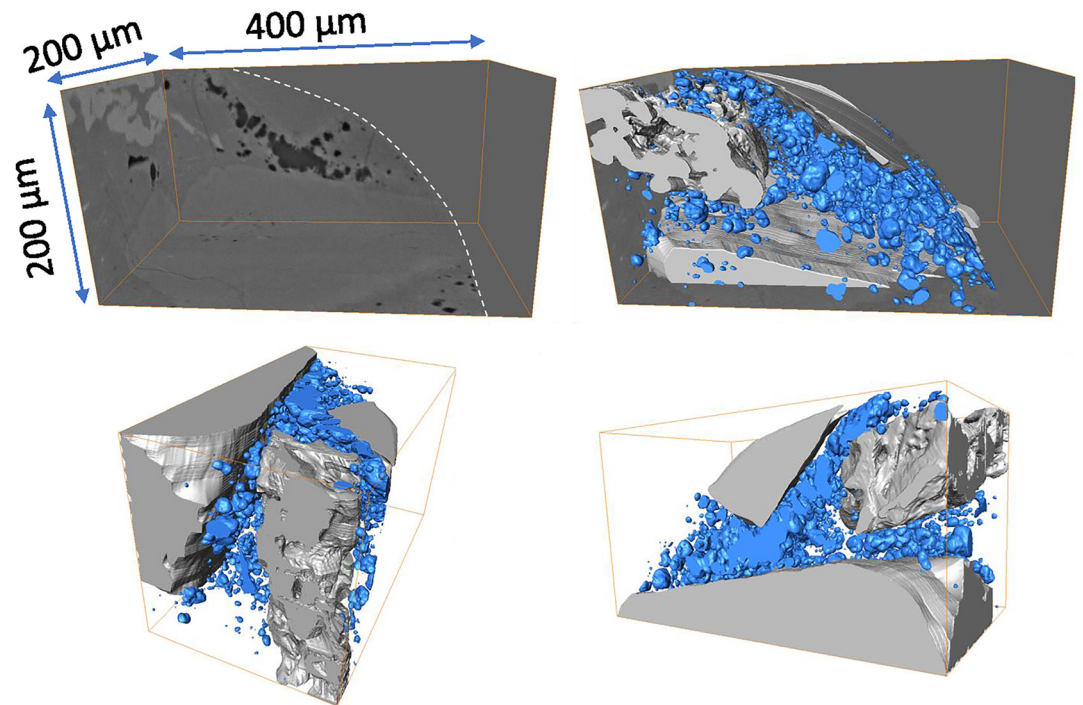
Figure 5. Synchrotron-based X-ray microtomography at a voxel size of 360 nm revealing the presence of a fourth vesicle type, forming vesicle trains along crystal boundaries, with vesicles and crystals represented in blue and gray in 3D renderings, respectively.

4. Discussion

We separate our discussion in two parts: (a) pre-fragmentation conditions prevailing in the dacitic magma prior to Vulcanian activity and (b) post-fragmentation vesiculation processes in the groundmass and the evolution of viscosity and growth rates during simultaneous cooling and degassing.

4.1. Pre-fragmentation Conditions in the Conduit

Projectile breadcrust bombs such as those studied here commonly have thick dense crusts that reflect cooling faster than bubble growth (Benage et al., 2014). The crust represents a snapshot of magma textural properties shortly before or at fragmentation due to rapid quenching that prevents further textural evolution. The population of large vesicles (Type 1) was formed prior to fragmentation. These large vesicles represent an initial porosity near zero (0.002) and an initial VND of $\sim 10^1$ mm^{-3}. Such small initial porosity is much lower than that predicted by equilibrium (Collombet et al., 2021) at the depth estimated for these breadcrust bombs (10–20 MPa equivalent to $\sim$400–800 m using a conduit density of 2,500 kg/m³; Wright et al., 2007), implying some outgassing process that reduced the porosity by gas escape and pore collapse during ascent and/or stalling at shallow levels in the plug. Several studies have shown that outgassing in crystal-rich magmas can occur deep in the conduit via channeling (e.g., Collombet et al., 2021; Crozier et al., 2022; Parmigiani et al., 2017). Initial (vesicle-free) phenocryst content in the breadcrust bombs is 40.1–41.5 vol% (Wright et al., 2023), which corresponds to the lower bound of the range favorable for channeling (40–70 vol%; Parmigiani et al., 2017). Additional outgassing processes in crystal-rich magmas include for instance shear deformation or simply the effect of rigid crystal network promoting deformation and coalescence (deGraffenried et al., 2019; Graham et al., 2023; Laumonier et al., 2011; Oppenheimer et al., 2015). Regardless of nature and timing of the outgassing process, the population of large, initially isolated vesicles was likely formed by collapse of an initially connected network of bubbles. Hence, the VND of Type 1 vesicles represent a minimum estimate of the VND achieved during ascent prior to collapse, since isolation of connected networks during collapse usually causes a decrease in number density (Martel & Iacono-Marziano, 2015). The VND of Type 1 vesicles before fragmentation is five to seven orders
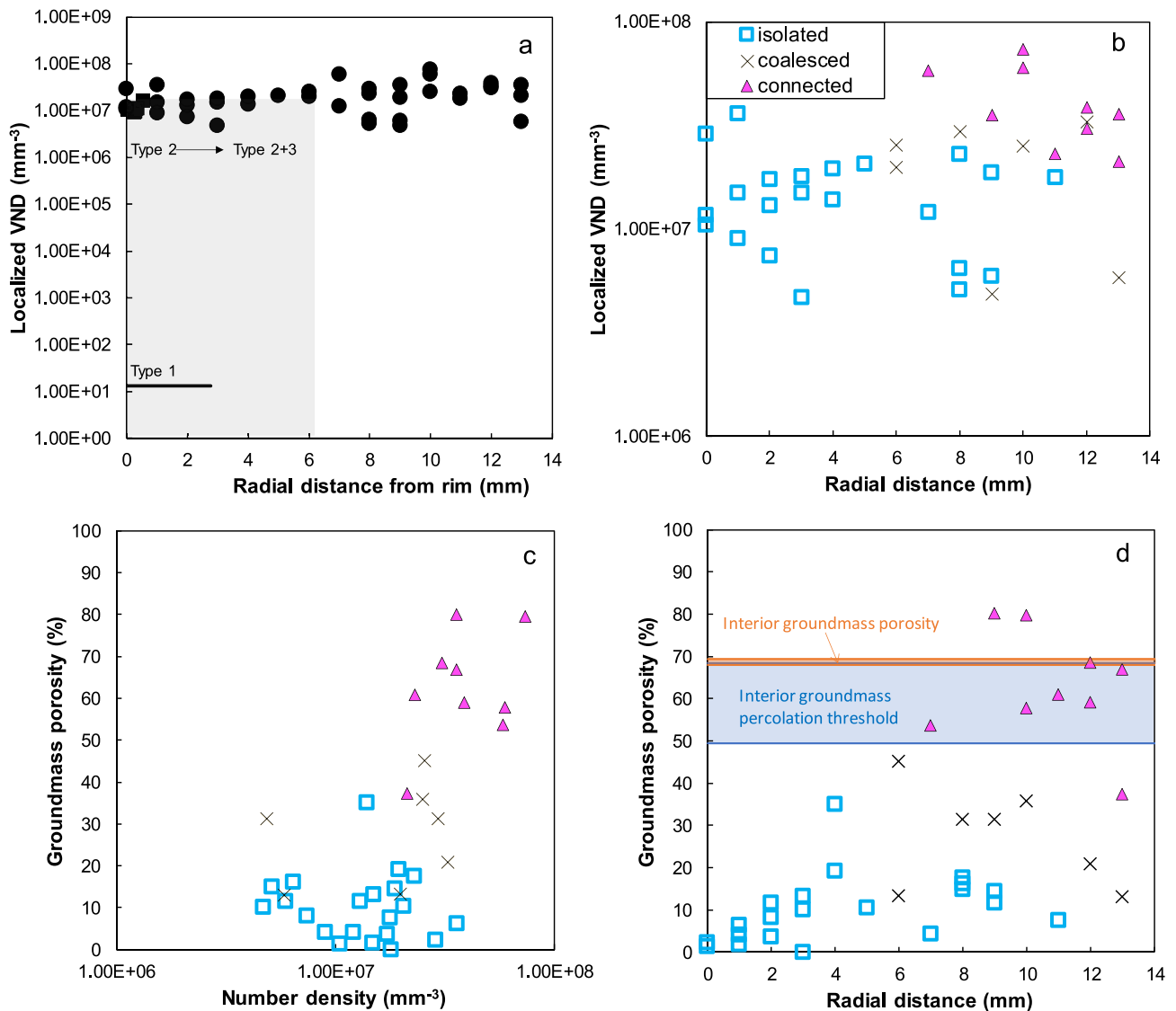
Figure 6. Vesicle number density (VND) and porosity as a function of radial distance to the crust (*R*) in breadcrust bomb GP8. (a) Localized VND values as a function of *R* for the large (Type 1) and small (Types 2 and 3) vesicle populations. The VND of large vesicles (black line) was measured using Synchrotron-based X-ray microtomography up to a distance of 2.75 mm from the crust. The gray shaded box corresponds to the range of radial positions where vesicle-free groundmass areas are observed. (b) Zoom in the range of VND values for the small vesicle populations (Type 2 and 3), with the distinction between isolated, coalesced and connected vesicles. (c) Groundmass porosity versus VND. (d) Groundmass porosity versus radial distance to the crust. Note that the connected vesicle networks identified in this study straddle the range of percolation threshold (from the percolation model of Giachetti et al., 2019) and connected porosities in the bomb interiors, both corrected for phenocryst content, from previous studies (Colombier et al., 2022; Wright et al., 2007).

of magnitude lower than final values that are preserved in pyroclasts after formation of Type 2 and 3 bubbles. The transition from low (10^1 mm^{-3}) to high (>10^6 mm^{-3}) VND from Type 1 to the nucleation of Type 2 bubbles corresponds to typical values expected for effusive (dome/plug emplacement) and explosive activity, respectively (Cáceres et al., 2020).

The halo of small vesicles around larger ones implies that these areas were enriched in H$_2$O prior to eruption, since Type 2 vesicles could nucleate before quenching whereas there was a nucleation delay for type 3 vesicles in the areas outside of these haloes near the crust. Such volatile enrichment and haloes of small vesicles around larger ones have been discussed for other types of pyroclasts such as rhyolitic obsidian pyroclasts at Chaitén volcano (Chile) (Browning et al., 2020), Mono Craters (USA) (Watkins et al., 2012), basaltic clasts at Kilauea volcano (Hawaii) (Carey et al., 2013), and has been attributed to bubble resorption caused by gas pressurization or cooling (Browning
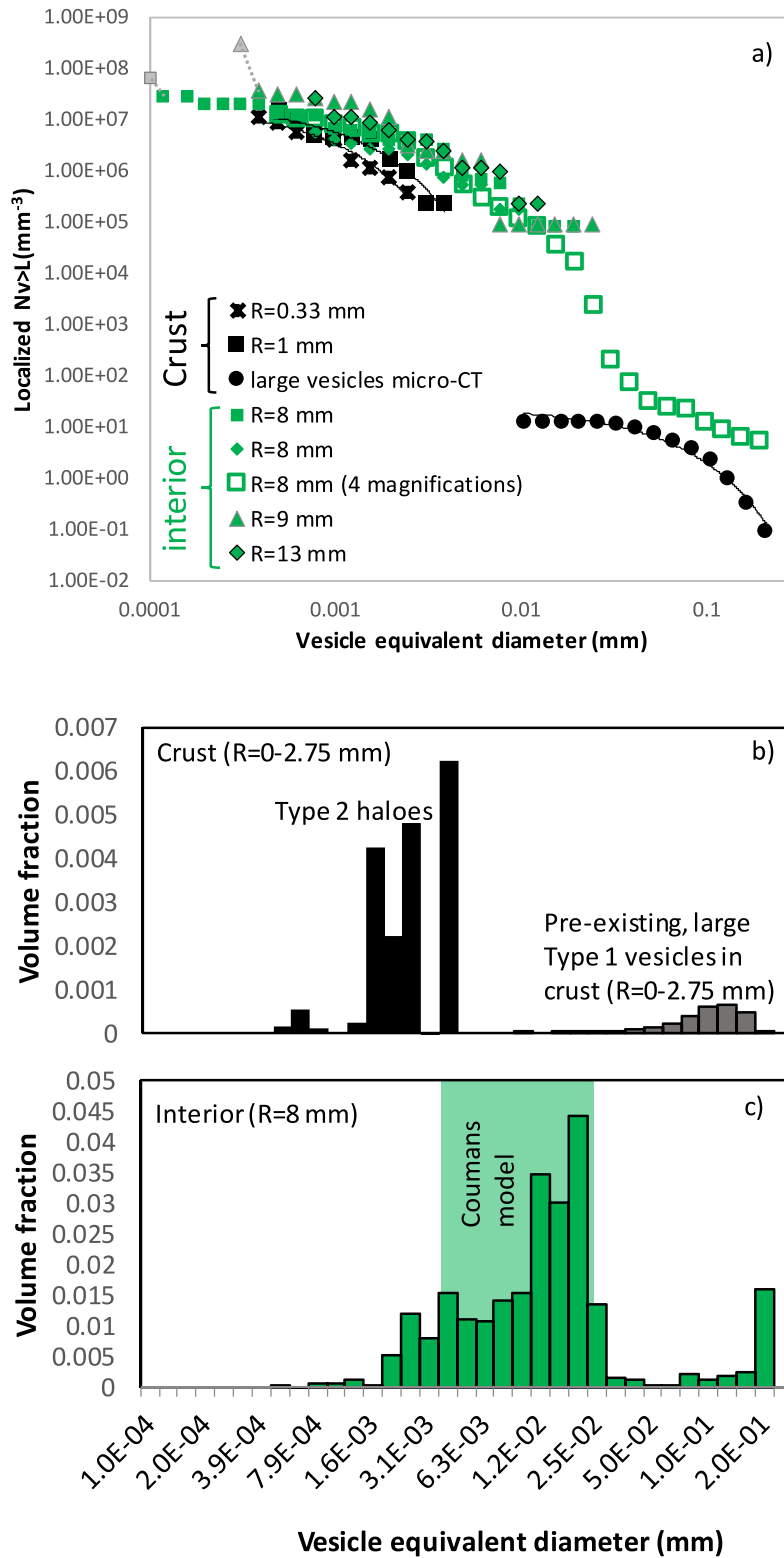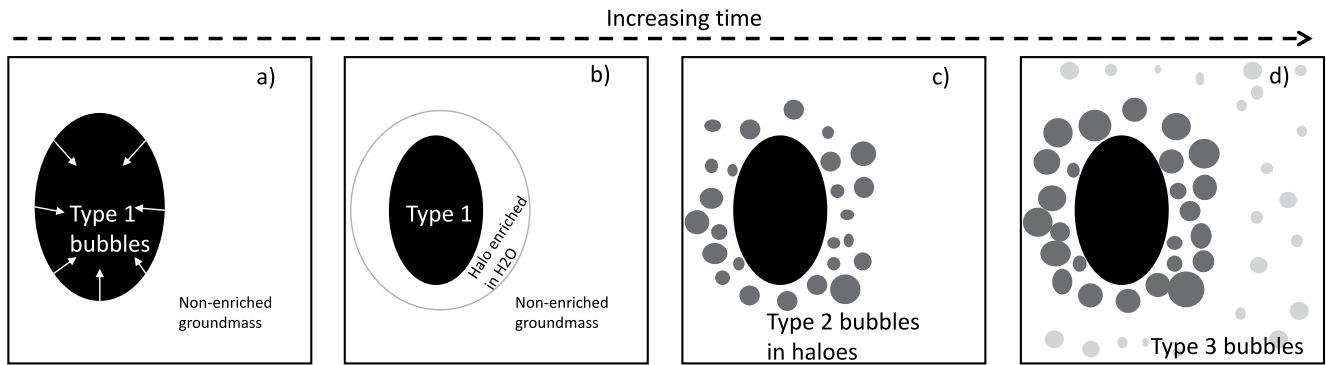
Figure 7.

Figure 8. Schematic representation of the evolution of bubble populations from pre-eruptive conditions to post-fragmentation processes. (a) Presence of large Type 1 isolated bubbles following collapse of an interconnected bubble network. Resorption of these isolated bubbles caused by pressurization. (b) Formation of a halo enriched in volatiles around these pressurized bubbles. (c) Nucleation and growth of Type 2 bubbles in these enriched haloes across the whole pyroclast. (d) Formation of Type 3 bubbles in more volatile-poor groundmass areas toward the core due to slower cooling and further growth of Type 2 bubbles.

et al., 2020; Carey et al., 2013; McIntosh et al., 2014). Garcia-Aristizabal et al. (2007) attributed seismicity and ground deformation signals at Guagua Pichincha during the 1999 Vulcanian activity to cyclic pressurization beneath the plug of the dome. Wright et al. (2023) recently presented additional textural and compositional evidence for such cyclic pressurization of the shallow conduit. There are multiple possible causes for increased pressure in the plug prior to Vulcanian explosive activity. For instance, it may arise from conduit replenishment by a volatile-rich (H_2O and CO_2) magma, continuous degassing and gas streaming from depth leading to overpressure in the degassed plug (Wright et al., 2007) or cessation of gas venting during plugging and dome formation (Clarke et al., 2015). Watkins et al. (2012) proposed that such textures can also be formed by pressure fluctuations linked to repeated fragmentation and annealing events. Additional causes of pressurization may be reduction of permeability in the upper parts of the plug by sealing of fractures by hydrothermal minerals (Stix et al., 1997) such as vapor-phase cristobalite (Boudon et al., 2015; Horwell et al., 2013) or welding in tuffisite veins (Kolzenburg et al., 2019).

Using the approach of Carey et al. (2013), we can estimate the timescale τ of pressurization from the distance over which water diffused during pressurization,

$$\delta \approx \sqrt{D\tau/5}$$

where δ is the thickness of the haloes and D is diffusivity of water obtained with the model of Zhang and Ni (2010) for a peraluminous rhyolitic melt using a temperature of 814°C (Samaniego et al., 2010), water content of 1.3 wt% (average value in the crust of GP8; Wright et al., 2007), and a pressure range of 10–20 MPa (Wright et al., 2007). We measured a range of thicknesses of 20–100 μm for the haloes, which yields a timescale of pressurization of 15 min to seven hours, lower than the time estimated for conduit refilling (in the order of days; Wright et al., 2007, 2023). We propose that the overpressure following replenishment, or pressurization induced by sealing of fractures and/or plug growth, created water-enriched haloes around large bubbles and fragmentation few minutes to hours after. Subsequent decompression led to nucleation and growth of type 2 bubbles in these volatile-enriched haloes. Figure 8 summarizes the timing of the pressurization process, enrichment of H_2O in the haloes and different nucleation and growth steps from vesicle populations 1 to 3.

4.2. Post-Fragmentation Evolution of the Dacitic Bombs

Understanding the evolution of a bubble network and associated volatile content inside breadcrust bombs after fragmentation is important to better understand cooling and transport processes (Benage et al., 2014). Such

Figure 7. Vesicle number density (VND) and size distributions (VSD) in breadcrust bomb GP8. (a) Cumulative VND distributions in the crust (black) and interior (green) of the bombs. Different symbols are used for different analyzed regions. The kink toward a high value of VND at the smallest bin size (gray data points) for $R = 8$ mm (green squares) and $R = 9$ mm (green triangles) is assumed to be related to an artifact at this high magnification and we chose the value of the plateau for a more accurate estimation of the number density in these cases. (b) VSD in the crust based on back-scattered electron (BSE) image and FOAMS analysis for small vesicles (mostly Type 2 at the given radial distances) and Synchrotron-based Micro-tomography and 3D image processing for large Type 1 vesicles. (c) VSD in the bomb interior based on BSE images and FOAMS analysis for all vesicle populations. The green shaded area corresponds to vesicle diameters obtained using the Coumans et al. (2020) bubble growth model. Note the different scales used for volume fraction pointing to a low porosity in the crust (b) and high porosity in the interior (c), with a bimodal VSD in both.
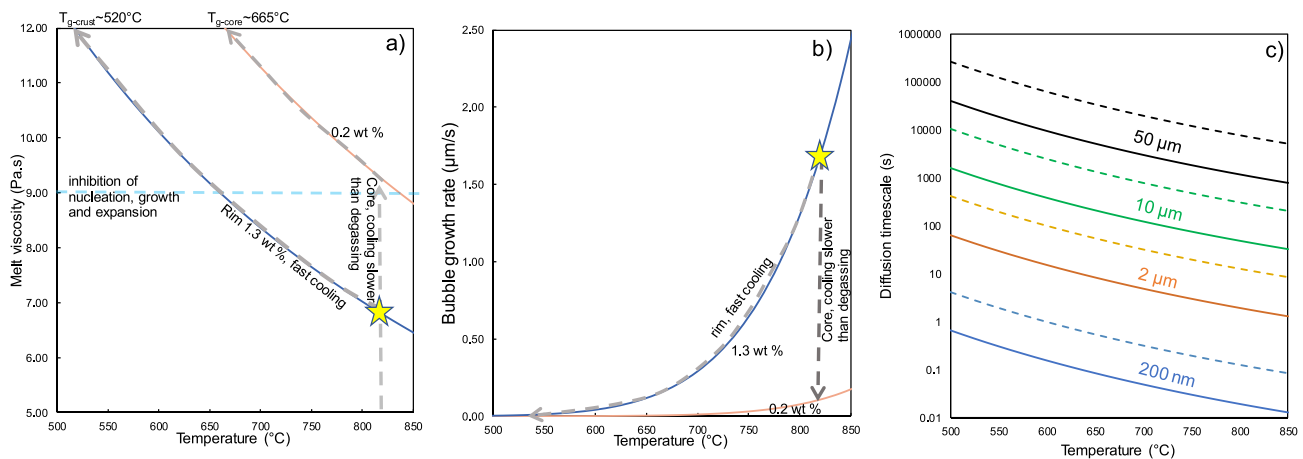
Figure 9. Modeled evolution of melt viscosity, bubble growth rate, and diffusion timescale with cooling and degassing in the crust and interior of the bombs. The yellow star corresponds to conditions at the time of fragmentation based on average water content preserved in the crust of GP8 (1.3 wt%; Wright et al., 2007) and eruptive temperature of 814°C (Samaniego et al., 2010). In (c), the dashed and solid lines correspond to water contents of 0.2 wt% (interior) and 1.3 wt% (crust), respectively.

products also provide a unique opportunity to study the temporal evolution of vesiculation in a natural, crystal-rich magma during both decompression and dwelling at atmospheric pressure, and complements experimental work on vesiculation in phenocryst- and microlite-bearing magmas (Cáceres et al., 2022; Graham et al., 2023). Finally, breadcrust bombs are unique volcanic rocks as their texture from the crust to the interior records the evolution from an isolated to a connected vesicle network, and hence can allow us to quantify the percolation threshold and onset of permeability (Colombier et al., 2017).

We model the evolution of viscosity in the groundmass rhyolitic melt (Wright et al., 2023) during fragmentation and subsequent vesiculation of the breadcrust bombs using the model of Hess and Dingwell (1996), appropriate for calcalkaline rhyolitic melts. The phenocryst-rich magma ascended from a depth of 5 km (Garcia-Aristizabal et al., 2007) to around 400–800 m based on pressure estimates of Wright et al. (2007) at a temperature $T_i \sim 814°C$ (Samaniego et al., 2010) and we assume for simplicity no temperature loss during this ascent, since decompression may induce either adiabatic cooling or heating via crystallization (Cashman & Blundy, 2000). During ascent up to fragmentation, degassing causes a reduction of H_2O content from around 4.5 wt% based on melt inclusions (Wright et al., 2023) down to 1.3 wt% (based on FTIR measurements in the crust of GP8; Wright et al., 2007). At the time of fragmentation, we assume that (a) the crust evolves dominantly by cooling down to the glass transition temperature (T_g is here approximated as the temperature at which viscosity is 10^{12} Pa.s; Giordano et al., 2008) due to rapid quenching (H_2O stays constant at 1.3 wt%), yielding $T_{g-crust} \sim 520°C$ (Figure 9a), and (b) the core stays hot at $T \sim T_i$ and viscosity increases here dominantly by degassing (Wilding et al., 1996) until the H_2O content drops down to 0.2 wt% (water content preserved in the core of GP8; Wright et al., 2007). Interestingly, the core reaches such water content at a viscosity of approximately 10^9 Pa.s, which is typically discussed as a viscosity threshold above which further nucleation and growth are inhibited by viscous retardation, the so-called "viscosity quench" (Barclay et al., 1995; Browning et al., 2020; Dingwell, 1998; Gardner & Denis, 2004; Thomas et al., 1994). Since no further vesiculation is possible, the core then further evolves by cooling along the 0.2 wt% H_2O viscosity curve and reaches T_{g-core} at around 665°C. These scenarios represent endmembers for the possible viscosity evolution of the crust and core. Between these two boundaries at intermediate radial position, all intermediate cases are expected for the viscosity evolution with temperature and water content depending on bubble growth rate and diffusion timescales. We also note that we have neglected potential heterogeneities in water content caused by pressurization and use average values for the water content in the crust and the core.

The η versus T evolution at different values of radial distance controls bubble growth rates along the radial profile. We use the empirical model of Browning et al. (2020) that relates growth rate to viscosity (and temperature) and calculate the evolution of growth rate in the crust and the core. In the rim, growth rate decreases mostly due to cooling whereas it decreases by degassing in the core (Figure 9b), as a consequence of the viscosity evolution. We therefore distinguish a dominant thermal quenching in the crust and a vesiculation-induced quench in the core as

proposed in other studies (Tuffen et al., 2022; Wilding et al., 1996). In the core, growth rate decreases as water is lost by nucleation and growth, and newly nucleated bubbles are therefore growing progressively more slowly as vesiculation continues. As a result, we can expect that Type 2 bubbles in the haloes around large bubbles grow faster than Type 3 bubbles.

Bubble growth rates depend on melt viscosity and the diffusion timescale which itself depends on bubble radius, pressure, temperature, and water content. We use the diffusion model of Zhang and Ni (2010) in a peraluminous rhyolitic melt to model bubble growth for different starting bubble radii based on our textural observations. The diffusion timescale is given by

$$\tau \sim R^2 / D$$

where R is the bubble radius and D is the diffusivity. Type 2 vesicles in the haloes have typical radii of $R = 200$ nm–2 μm. At pre-eruptive conditions ($T_i \sim 814°C$, $H_2O \sim 1$–1.3wt%), the diffusion timescale is very low for such bubble sizes (Figure 9c) and bubble growth rate is fast (Figure 9b). This implies that the cooling timescale must be even smaller (i.e., quasi-instantaneous quenching) in order to prevent rapid vesiculation and preserve such small vesicles after fragmentation. These vesicles are hence the remnants of mostly syn-fragmentation bubble nucleation and had no time to grow larger due to fast quenching in the crust. $R \sim 10$ μm corresponds to the peak of the small vesicle population (including both Type 2 and 3) preserved toward the core (Figure 7c). The diffusion timescale is significantly longer (on the order of minutes) so these bubbles could only grow this large in the interior of the bombs due to slow cooling. Finally, $R = 50$ μm corresponds to the average radius of large, pre-eruptive bubbles (Type 1) preserved in the crust and the range of diffusion timescales for these is around 15 min to 2 hr depending on the water content. These large diffusion timescales for Type 1 bubbles confirm that they must be formed prior to fragmentation and cooling. The water content around these large bubbles after complete vesiculation of Type 2 bubbles is likely depleted so that the diffusion timescale is more toward the higher end of this range. Larger diameters observed for these vesicles toward the core may be better explained by (i) expansion or (ii) growth by coalescence of Type 2 bubbles in the halo with the large bubbles, rather than diffusion due to these very long diffusion timescales.

The radial textural evolution observed here informs us on post-fragmentation vesiculation in the phenocryst- and microlite-bearing magma and on the transition from closed- to open-system degassing at a micro-scale. From our textural analysis, we observe that vesiculation during or following fragmentation is a highly localized process, resulting in heterogenous textures both parallel and perpendicular to the bomb surface (Figures 1, 2 and 6; Wright et al., 2007). As discussed above, haloes of small Type 2 vesicles must be formed during fragmentation since quenching of the crust is very rapid. Type 3 vesicles are likely formed shortly after in areas that remained above the glass transition temperature from intermediate radial positions toward the core. Both Type 2 and 3 vesicles are characterized by high number density likely reflecting the high syn-explosive decompression rates (Figure 6; Toramaru, 2006). We note that most of the VND data for the breadcrust bombs exceed values from the literature for other silicic eruptions (see Jutzeler et al., 2016 for a compilation). Colombier et al. (2022) also reported high values for VND at 10^8 mm^{-3} for pumice from Plinian activity at Guagua Pichincha. These high values can be better explained by the methodology used in our study and in Colombier et al. (2022) in which we focus on localized values of the VND and not average values across heterogenous samples. However, we emphasize that one distribution with four magnifications and four different areas of the sample at the highest magnification also yielded high vesicle number densities of 10^7 mm^{-3}.

Isolated bubbles dominate in the crust ($R < 6$ mm) and then transition to coalesced clusters and finally to an interconnected bubble network in the bomb core. The porosity window at which this transition occurs straddles previous estimates of the percolation threshold in these breadcrust bombs (Colombier et al., 2022). The fact that percolating areas occur only for $R > 6$ mm where vesicle-free groundmass does not exist anymore suggests that this radial distance is a threshold between an isolated bubble system in the crust and a percolating bubble network in the interior. At larger scales than the groundmass, it is important to keep in mind that pore connectivity also occurs via cracks and voids in these samples, even where isolated bubbles dominate.

We used the model of Coumans et al. (2020) to simulate the evolution of bubble growth during decompression (Figure 10). As input, we use the solubility model of Ryan et al. (2015), the diffusivity model of Zhang and Ni (2010), the viscosity model of Hess and Dingwell (1996), a cooling time of approximately 1,000 s (based on the dimensions of the bombs studied here and the cooling model of Colombier et al., 2018), and we choose
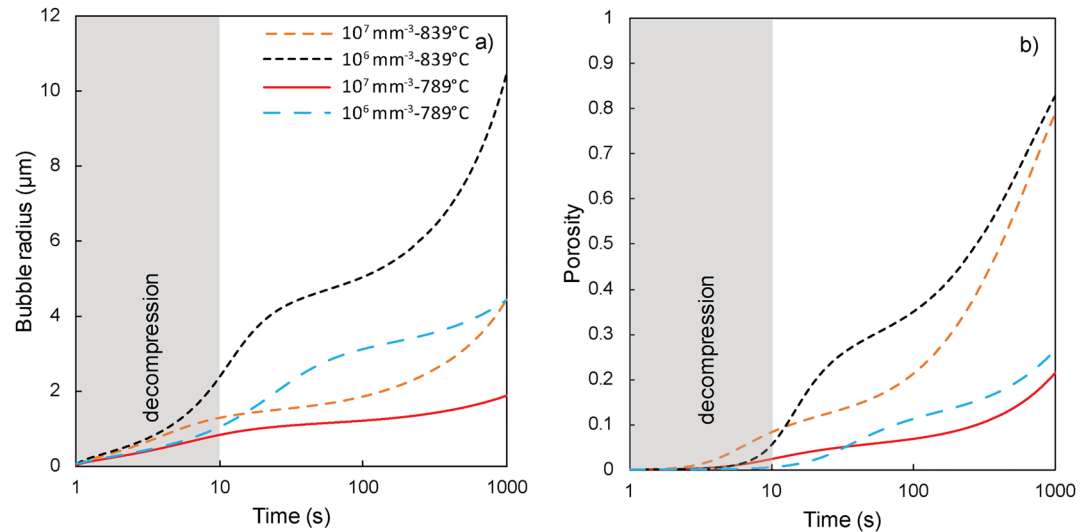
Figure 10. Output of the Coumans et al. (2020) bubble growth model applied to the bomb GP8 showing the evolution of bubble radius and gas volume fraction with time for different starting conditions (see text). The gray shaded area corresponds to the first step of vesiculation during decompression.

isothermal conditions during decompression from 20 MPa of a rhyolitic melt with 1.3 wt% water, and at a rate of 2 MPa/s based on previous ejection velocity estimates of 77 m/s (Wright et al., 2007). We set a temperature range of 814 ± 25 (789–839) °C (Samaniego et al., 2010) and an initial VND range of 10^{6-7} mm^{-3} based on our textural data. The model results in bubble growth during both decompression of the bomb and isothermal dwell at atmospheric pressure, with an increase in bubble diameter up to a range of 3.5–22 μm (Figure 10a), consistent with the mode of small vesicles in the bomb interior (Figure 7c), and an increase of gas volume fraction up to 0.20–0.80 (Figure 10b), in agreement with most groundmass porosity values measured in the interior (data at $R > 8$ mm in Figure 6d). Instead of the range in temperature used as input in the model, we expect that the observed range of bubble sizes, VND and porosity values in the bomb interior arise from differences in nucleation time during continuous nucleation and growth, and variable local water content such as in the haloes.

5. Conclusions

Textural analysis of breadcrust bombs yields insights into pre- to post-fragmentation processes during the 1999 Vulcanian activity at Guagua Pichincha volcano, Ecuador. Large isolated vesicles preserved in the crust are evidence for a pre-eruptive episode of outgassing and bubble collapse. Haloes of Type 2, small vesicles around these large ones imply enrichment of H_2O in these haloes via a pressurization process occurring minutes to hours prior to fragmentation. Post-fragmentation vesiculation in the groundmass, and the transition from closed- to open-system degassing toward the core, is a highly localized process and matches our previous study on the percolation threshold of Guagua Pichincha dacites (Colombier et al., 2022). Finally, we conclude that thermal quenching is the dominant process in the crust of breadcrust bombs due to rapid cooling, whereas quenching is dominated by outgassing in the bomb's interior.

This study may contribute to the interpretation of vesicle textures in the light of seismic and ground deformation signals during Vulcanian eruptions. Our results may also be used in cooling and transport models of breadcrust bombs by incorporating the effect of post-fragmentation degassing, and in a broader context to better understand the highly localized nature of vesiculation and permeability development in phenocryst- and microlite-bearing silicic magmas.

Data Availability Statement

Vesicle number density and vesicle size distribution data are available at Colombier et al. (2023).

References

Barclay, J., Riley, D. S., & Sparks, R. S. J. (1995). Analytical models for bubble growth during decompression of high viscosity magmas. *Bulletin of Volcanology*, *57*(6), 422–431. https://doi.org/10.1007/BF00300986

Benage, M. C., Dufek, J., Degruyter, W., Geist, D., Harpp, K., & Rader, E. (2014). Tying textures of breadcrust bombs to their transport regime and cooling history. *Journal of Volcanology and Geothermal Research*, *274*, 92–107. https://doi.org/10.1016/j.jvolgeores.2014.02.005

Blower, J. D., Keating, J. P., Mader, H. M., & Phillips, J. C. (2003). The evolution of bubble size distributions in volcanic eruptions. *Journal of Volcanology and Geothermal Research*, *120*(1–2), 1–23. https://doi.org/10.1016/S0377-0273(02)00404-3

Boudon, G., Balcone-Boissard, H., Villemant, B., & Morgan, D. J. (2015). What factors control superficial lava dome explosivity? *Scientific Reports*, *5*(1), 14551. https://doi.org/10.1038/srep14551

Browning, J., Tuffen, H., James, M. R., Owen, J., Castro, J. M., Halliwell, S., & Wehbe, K. (2020). Post-fragmentation vesiculation timescales in hydrous rhyolitic bombs from Chaitén volcano. *Journal of South American Earth Sciences*, *104*, 102807. https://doi.org/10.1016/j.jsames.2020.102807

Cáceres, F., Scheu, B., Colombier, M., Hess, K. U., Feisel, Y., Ruthensteiner, B., & Dingwell, D. B. (2022). The roles of microlites and phenocrysts during degassing of silicic magma. *Earth and Planetary Science Letters*, *577*, 117264. https://doi.org/10.1016/j.epsl.2021.117264

Cáceres, F., Wadsworth, F. B., Scheu, B., Colombier, M., Madonna, C., Cimarelli, C., et al. (2020). Can nanolites enhance eruption explosivity? *Geology*, *48*(10), 997–1001. https://doi.org/10.1130/G47317.1

Carey, R. J., Manga, M., Degruyter, W., Gonnermann, H., Swanson, D., Houghton, B., et al. (2013). Convection in a volcanic conduit recorded by bubbles. *Geology*, *41*(4), 395–398. https://doi.org/10.1130/G33685.1

Cashman, K., & Blundy, J. (2000). Degassing and crystallization of ascending andesite and dacite. *Philosophical Transactions of the Royal Society of London,Series A: Mathematical, Physical and Engineering Sciences*, *358*(1770), 1487–1513. https://doi.org/10.1098/rsta.2000.0600

Clarke, A. B., Ongaro, T. E., & Belousov, A. (2015). Vulcanian eruptions. In *The encyclopedia of volcanoes* (pp. 505–518). Academic Press. https://doi.org/10.1016/B978-0-12-385938-9.00028-6

Collombet, M., Burgisser, A., Colombier, M., & Gaunt, E. (2021). Evidence for deep gas loss in open volcanic systems. *Bulletin of Volcanology*, *83*(2), 1–16. https://doi.org/10.1007/s00445-020-01433-0

Colombier, M., Bernard, B., Wright, H., Le Pennec, J. L., Cáceres, F., Cimarelli, C., et al. (2022). Conduit processes in crystal-rich dacitic magma and implications for eruptive cycles at Guagua Pichincha volcano, Ecuador. *Bulletin of Volcanology*, *84*(12), 105. https://doi.org/10.1007/s00445-022-01612-1

Colombier, M., Manga, M., Wright, H., Bernard, B., DeGraffenried, R., Cáceres, F., et al. (2023). 2D and 3D textural analysis of vesicles in breadcrust bombs from the 1999 Vulcanian activity at Guagua Pichincha Volcano, Ecuador, version 1.0 [Dataset]. Interdisciplinary Earth Data Alliance (IEDA). https://doi.org/10.26022/IEDA/112846

Colombier, M., Scheu, B., Wadsworth, F. B., Cronin, S., Vasseur, J., Dobson, K. J., et al. (2018). Vesiculation and quenching during Surtseyan eruptions at Hunga Tonga-Hunga Ha'apai Volcano, Tonga. *Journal of Geophysical Research: Solid Earth*, *123*(5), 3762–3779. https://doi.org/10.1029/2017JB015357

Colombier, M., Wadsworth, F. B., Gurioli, L., Scheu, B., Kueppers, U., Di Muro, A., & Dingwell, D. B. (2017). The evolution of pore connectivity in volcanic rocks. *Earth and Planetary Science Letters*, *462*, 99–109. https://doi.org/10.1016/j.epsl.2017.01.011

Coumans, J. P., Llewellin, E. W., Wadsworth, F. B., Humphreys, M. C. S., Mathias, S. A., Yelverton, B. M., & Gardner, J. E. (2020). An experimentally validated numerical model for bubble growth in magma. *Journal of Volcanology and Geothermal Research*, *402*, 107002. https://doi.org/10.1016/j.jvolgeores.2020.107002

Crozier, J., Tramontano, S., Forte, P., Oliva, S. J. C., Gonnermann, H. M., Lev, E., et al. (2022). Outgassing through magmatic fractures enables effusive eruption of silicic magma. *Journal of Volcanology and Geothermal Research*, *430*, 107617. https://doi.org/10.1016/j.jvolgeores.2022.107617

de Graffenried, R. L., Larsen, J. F., Graham, N. A., & Cashman, K. V. (2019). The influence of phenocrysts on degassing in crystal-bearing magmas with rhyolitic groundmass melts. *Geophysical Research Letters*, *46*(10), 5127–5136. https://doi.org/10.1029/2018GL081822

Dingwell, D. B. (1998). Magma degassing and fragmentation: Recent experimental advances. From magma to tephra-modelling physical processes of explosive volcanic eruptions.

Druitt, T. H., Young, S. R., Baptie, B., Bonadonna, C., Calder, E. S., Clarke, A. B., et al. (2002). Episodes of cyclic Vulcanian explosive activity with fountain collapse at Soufrière Hills Volcano. *Montserrat*, *21*(1), 281–306. https://doi.org/10.1144/GSL.MEM.2002.021.01.13

Garcia-Aristizabal, A., Kumagai, H., Samaniego, P., Mothes, P., Yepes, H., & Monzier, M. (2007). Seismic, petrologic, and geodetic analyses of the 1999 dome-forming eruption of Guagua Pichincha volcano, Ecuador. *Journal of Volcanology and Geothermal Research*, *161*(4), 333–351. https://doi.org/10.1016/j.jvolgeores.2006.12.007

Gardner, J. E., & Denis, M. H. (2004). Heterogeneous bubble nucleation on Fe-Ti oxide crystals in high-silica rhyolitic melts. *Geochimica et Cosmochimica Acta*, *68*(17), 3587–3597. https://doi.org/10.1016/j.gca.2004.02.021

Giachetti, T., Burgisser, A., Arbaret, L., Druitt, T. H., & Kelfoun, K. (2011). Quantitative textural analysis of Vulcanian pyroclasts (Montserrat) using multi-scale X-ray computed microtomography: Comparison with results from 2D image analysis. *Bulletin of Volcanology*, *73*(9), 1295–1309. https://doi.org/10.1007/s00445-011-0472-1

Giachetti, T., Druitt, T. H., Burgisser, A., Arbaret, L., & Galven, C. (2010). Bubble nucleation, growth and coalescence during the 1997 Vulcanian explosions of Soufrière Hills Volcano, Montserrat. *Journal of Volcanology and Geothermal Research*, *193*(3–4), 215–231. https://doi.org/10.1016/j.jvolgeores.2010.04.001

Giachetti, T., Gonnermann, H. M., Gardner, J. E., Burgisser, A., Hajimirza, S., Earley, T. C., et al. (2019). Bubble coalescence and percolation threshold in expanding rhyolitic magma. *Geochemistry, Geophysics, Geosystems*, *20*(2), 1054–1074. https://doi.org/10.1029/2018GC008006

Giordano, D., Russell, J. K., & Dingwell, D. B. (2008). Viscosity of magmatic liquids: A model. *Earth and Planetary Science Letters*, *271*(1–4), 123–134. https://doi.org/10.1016/j.epsl.2008.03.038

Graham, N. A., Larsen, J. F., Tasa, K. Y., de Graffenried, R. L., Cashman, K. V., & McCartney, K. N. (2023). Controls of crystal shape on degassing mechanisms in crystal-rich magmas with rhyolitic groundmass melts. *Earth and Planetary Science Letters*, *601*, 117891. https://doi.org/10.1016/j.epsl.2022.117891

Hess, K. U., & Dingwell, D. B. (1996). Viscosities of hydrous leucogranitic melts: A non-Arrhenian model. *American Mineralogist: Journal of Earth and Planetary Materials*, *81*(9–10), 1297–1300.

Horwell, C. J., Williamson, B. J., Llewellin, E. W., Damby, D. E., & Le Blond, J. S. (2013). The nature and formation of cristobalite at the Soufrière Hills volcano, Montserrat: Implications for the petrology and stability of silicic lava domes. *Bulletin of Volcanology*, *75*(3), 1–19. https://doi.org/10.1007/s00445-013-0696-3

Jutzeler, M., White, J. D., Proussevitch, A. A., & Gordee, S. M. (2016). Vesiculation and fragmentation history in a submarine scoria cone-forming eruption, an example from Nishiizu (Izu Peninsula, Japan). *Bulletin of Volcanology*, *78*(2), 1–25. https://doi.org/10.1007/s00445-016-0999-2

Kolzenburg, S., Ryan, A. G., & Russell, J. K. (2019). Permeability evolution during non-isothermal compaction in volcanic conduits and tuffisite veins: Implications for pressure monitoring of volcanic edifices. *Earth and Planetary Science Letters*, *527*, 115783. https://doi.org/10.1016/j.epsl.2019.115783

Laumonier, M., Arbaret, L., Burgisser, A., & Champallier, R. (2011). Porosity redistribution enhanced by strain localization in crystal-rich magmas. *Geology*, *39*(8), 715–718. https://doi.org/10.1130/G31803.1

Martel, C., & Iacono-Marziano, G. (2015). Timescales of bubble coalescence, outgassing, and foam collapse in decompressed rhyolitic melts. *Earth and Planetary Science Letters*, *412*, 173–185. https://doi.org/10.1016/j.epsl.2014.12.010

McIntosh, I. M., Llewellin, E. W., Humphreys, M. C. S., Nichols, A. R. L., Burgisser, A., Schipper, C. I., & Larsen, J. F. (2014). Distribution of dissolved water in magmatic glass records growth and resorption of bubbles. *Earth and Planetary Science Letters*, *401*, 1–11. https://doi.org/10.1016/j.epsl.2014.05.037

Oppenheimer, J., Rust, A. C., Cashman, K. V., & Sandnes, B. (2015). Gas migration regimes and outgassing in particle-rich suspensions. *Frontiers in Physics*, *3*, 60. https://doi.org/10.3389/fphy.2015.00060

Parmigiani, A., Degruyter, W., Leclaire, S., Huber, C., & Bachmann, O. (2017). The mechanics of shallow magma reservoir outgassing. *Geochemistry, Geophysics, Geosystems*, *18*(8), 2887–2905. https://doi.org/10.1002/2017GC006912

Ryan, A. G., Russell, J. K., Nichols, A. R., Hess, K. U., & Porritt, L. A. (2015). Experiments and models on H_2O retrograde solubility in volcanic systems. *American Mineralogist*, *100*(4), 774–786. https://doi.org/10.2138/am-2015-5030

Samaniego, P., Robin, C., Chazot, G., Bourdon, E., & Cotten, J. (2010). Evolving metasomatic agent in the Northern Andean subduction zone, deduced from magma composition of the long-lived Pichincha volcanic complex (Ecuador). *Contributions to Mineralogy and Petrology*, *160*(2), 239–260. https://doi.org/10.1007/s00410-009-0475-5

Shea, T., Houghton, B. F., Gurioli, L., Cashman, K. V., Hammer, J. E., & Hobden, B. J. (2010). Textural studies of vesicles in volcanic rocks: An integrated methodology. *Journal of Volcanology and Geothermal Research*, *190*(3–4), 271–289. https://doi.org/10.1016/j.jvolgeores.2009.12.003

Stix, J., Torres, R. C., Narváez, L., Raigosa, J. A., Gómez, D., & Castonguay, R. (1997). A model of vulcanian eruptions at Galeras volcano, Colombia. *Journal of Volcanology and Geothermal Research*, *77*(1–4), 285–303. https://doi.org/10.1016/S0377-0273(96)00100-X

Thomas, N., Jaupart, C., & Vergniolle, S. (1994). On the vesicularity of pumice. *Journal of Geophysical Research*, *99*(B8), 15633–15644. https://doi.org/10.1029/94JB00650

Toramaru, A. (2006). BND (bubble number density) decompression rate meter for explosive volcanic eruptions. *Journal of Volcanology and Geothermal Research*, *154*(3–4), 303–316. https://doi.org/10.1016/j.jvolgeores.2006.03.027

Tuffen, H., Farquharson, J. I., Wadsworth, F. B., Webb, C., Owen, J., Castro, J. M., et al. (2022). Mid-loaf crisis: Internal breadcrust surfaces in rhyolitic pyroclasts reveal dehydration quenching. *Geology*, *50*(9), 1058–1062. https://doi.org/10.1130/G49959.1

Watkins, J. M., Manga, M., & DePaolo, D. J. (2012). Bubble geobarometry: A record of pressure changes, degassing, and regassing at Mono Craters, California. *Geology*, *40*(8), 699–702. https://doi.org/10.1130/G33027.1

Wilding, M., Webb, S., Dingwell, D., Ablay, G., & Marti, J. (1996). Cooling rate variation in natural volcanic glasses from Tenerife, Canary Islands. *Contributions to Mineralogy and Petrology*, *125*(2–3), 151–160. https://doi.org/10.1007/s004100050212

Wright, H. M., Cashman, K. V., Rosi, M., & Cioni, R. (2007). Breadcrust bombs as indicators of Vulcanian eruption dynamics at Guagua Pichincha volcano, Ecuador. *Bulletin of Volcanology*, *69*(3), 281–300. https://doi.org/10.1007/s00445-006-0073-6

Wright, H. M. N., Cioni, R., Cashman, K. V., Mothes, P., & Rosi, M. (2023). Decompression and degassing, repressurization, and regassing during cyclic eruptions at Guagua Pichincha volcano, Ecuador, 1999–2001. *Bulletin of Volcanology*, *85*(2), 12. https://doi.org/10.1007/s00445-023-01626-3

Zhang, Y., & Ni, H. (2010). Diffusion of H, C, and O components in silicate melts. *Reviews in Mineralogy and Geochemistry*, *72*(1), 171–225. https://doi.org/10.2138/rmg.2010.72.5